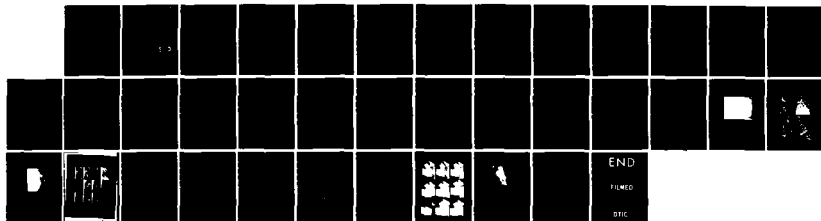
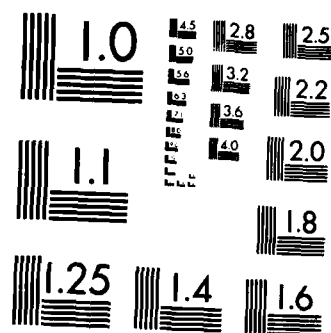


AD-A154 870 THE MEASUREMENT OF STRAIN FIELDS BY X-RAY TOPOGRAPHIC 1/1
CONTOUR MAPPING(U) ILLINOIS UNIV AT URBANA DEPT OF
METALLURGY AND MINING ENGINEERING S R STOCK ET AL.
UNCLASSIFIED MAY 85 N00014-83-K-0468 F/G 13/13 NL





MICROCOPY RESOLUTION TEST CHART
NATIONAL BUREAU OF STANDARDS-1963-A

AD-A154 870

(10) *ETH*

THE MEASUREMENT OF STRAIN FIELDS BY X-RAY TOPOGRAPHIC CONTOUR MAPPING

S.R. Stock, Haydn Chen and H.K. Birnbaum

University of Illinois
Department of Metallurgy
Urbana, IL 61801

Technical Report

May 1985

DTIC
ELECTE
JUN 12 1985
S B

DTIC FILE COPY

This document is unclassified. Reproduction and distribution for any purpose of the U.S. government is permitted.

DISTRIBUTION STATEMENT A

Approved for public release
Distribution Unlimited

85 5 31 002

THE MEASUREMENT OF STRAIN FIELDS BY
X-RAY TOPOGRAPHIC CONTOUR MAPPING

S. R. Stock*, Haydn Chen and H. K. Birnbaum

Department of Metallurgy and Mining Engineering
University of Illinois at Urbana-Champaign
Urbana, Illinois 61801 USA

*Now at the School of Materials Engineering, Georgia Institute
of Technology, Atlanta, Georgia 30332-0100 USA.

ABSTRACT

An x-ray topographic method is described for measuring the magnitude of the components of the strain tensor as a function of position in single crystal specimens. Several variants of the technique are described for use with monochromatic or white x-radiation. Results are reported for some components of the deformation field surrounding a precipitate of β -NbH. Possible applications of contour mapping are discussed.

Accession For	
NTIS SP441	
NTIS 541	
Unpublished	
Classification	
PER LETTER	
By	
Approved by	
Approved by	
Dissemination	
A-1	



I. INTRODUCTION

X-ray diffraction topography offers unique advantages for imaging dislocations and accumulated plastic deformation in single crystals. X-ray diffraction is much more sensitive to strains and samples larger volumes of material than does electron microscopy. Also, topography can be used non-destructively to examine a single specimen many times during the course of an experiment. With the advent of synchrotron radiation sources and of rapid imaging systems for laboratory sources, the emphasis in applying x-ray topography is shifting from characterization studies to dynamic, in-situ observation of experiments. One such application is observation of plastic deformation during tensile or bending tests. Most topographic studies of plastic deformation, however, have been confined to situations where individual dislocations or slip bands can still be resolved (dislocation densities $< 10^6 \text{ cm}^{-2}$). Extension of x-ray topographic methods to crystals with higher dislocation densities would be an important step in the study of relatively small amounts of plastic deformation which, for example, characterize the early stages of yielding.

One means is to measure the rocking curve width on a point-by-point basis and use these measurements to map the distribution of deformation (Liu, Weng and Weissmann 1982). Alternatively, equi-inclination contours (analogues to bend contours in electron microscopy) can be used. Such contours are well known (Renninger

1965 and Jacobs and Hart 1977), and in the present paper we use them to determine the spatial distribution of strain fields. Sets of equi-inclination contours, obtained with different diffraction vectors and rotation axes, allow one to measure the components of strain as a function of position. Methods are developed for monochromatic and synchrotron white radiation sources and are used to study the strain field surrounding a precipitate of β -NbH in a niobium single crystal.

II. CONTOUR MAPPING

Consider a strain center which deforms a thin, ribbon-like single crystal and at which is located the origin of a rectilinear coordinate system (Figure 1). Diffraction from planes normal to axis \underline{x}_i , denoted by P_i , will be considered for the case of a parallel, spatially-broad and monochromatic beam of x-rays. Variations in the interplanar spacing or in the orientation of the diffracting planes P_i will limit diffraction to a portion of the specimen for each angular setting of the crystal. Only changes in the displacement u_i (normal to P_i) will change the diffraction conditions, i.e., the terms $\partial u_i / \partial x_j$ are related to the rotation of the specimen relative to the beam of x-rays. The rotation about \underline{x}_k which is required to align the deformed planes of a new region for diffraction is denoted by $\Delta \omega_i^k(l, l+1)$. The superscript k defines the experimental rotation axis \underline{x}_k , the subscript i denotes the diffraction plane, P_i , and the arguments l and $l+1$ identify the spatial

positions of the two volumes of material aligned for diffraction before and after the rotation is applied.

One of the terms $\partial u_i / \partial x_j$ is a dilational strain $\partial u_i / \partial x_i$, and the other two are parts of shear strains. Each of the terms $\partial u_i / \partial x_j$ will contribute separately to $\Delta \omega_i^k$, and the form of the contributions to $\Delta \omega_i^k$ are well known (Hart 1981 and Bonse and Hartmann 1981). The change in the Bragg angle $\Delta \theta_D$ from the varying dilational field is related to the change in $\partial u_i / \partial x_i$ from position l to $l+1$ through the differential form of Bragg's law:

$$\Delta d / d_0 = -\Delta \theta_D \cot \theta_0 = \Delta \epsilon_{11} = \frac{\partial u_i(l+1, l)}{\partial x_i}, \quad (1)$$

where Δd is the change in spacing of the diffraction planes, d_0 is the plane spacing of the undeformed specimen and θ_0 is the Bragg angle for the undeformed crystal. The shear terms $\partial u_i / \partial x_m$ and $\partial u_i / \partial x_k$ represent tilting of planes P_i about axes \underline{x}_k and \underline{x}_m , respectively.* For rotation axis \underline{x}_k , $\partial u_i / \partial x_m$ is identical to the angle $\Delta \theta_S$ through which the crystal must be rotated. Consideration of geometry shows that the contribution of $\partial u_i / \partial x_k$ to $\Delta \omega_i^k$ is much less than that of either $\partial u_i / \partial x_i$ or $\partial u_i / \partial x_m$.

It is generally convenient to choose a reference position which has suffered no deformation from the strain center.

*Each of the directions \underline{x}_i , \underline{x}_k and \underline{x}_m represents a different coordinate axis.

Strains and rotations are measured relative to the values at this position, and the nomenclature can be simplified considerably:

$$\omega_i^k(l) = \frac{\partial u_i(l)}{\partial x_m} - \frac{\partial u_i(l)}{\partial x_i} \tan \theta_0 \quad (2)$$

where l indicates the volume element of diffracting material.

In x-ray topographs of deformed crystals recorded using monochromatic radiation, the limited volume which can diffract at any angular setting produces narrow bands of increased diffracted intensity. These contours are termed equi-inclination contours. Since the position of the diffracting volume will vary with the angular setting of the crystal, the position of an equi-inclination contour may be mapped as a function of crystal rotation using multiple exposures of a single piece of film or a set of singly exposed emulsions. Characteristic radiation or monochromatized synchrotron radiation may be used to produce the equi-inclination contours. Similar contours (termed absorption edge contours) may be produced with synchrotron white radiation by orienting the deformed crystal so that it diffracts a range of wavelengths on either side of the absorption edge of an element in the specimen crystal. The absorption edge contour is quite prominent in x-ray topographs because of the differing absorption coefficients on either side of the edge. Examples of both types of contour mapping are presented below.

An illustration of the relationship between contour positions (equi-inclination or absorption edge) and rotation

appears in Figure 1. It shows a number of contours between the strain center and the unstrained portion of the crystal. One may plot the cumulative rotation from the undeformed region to the position of the l^{th} contour, $\omega_i^k(l)$, as a function the separation along \underline{x}_i between the contour and the strain center (Figure 1b). The measurement is repeated along each line of constant x_k to determine rotation as a function of position. Transmission topography, however, allows only the measurement of the two dimensional variation of strain since it averages over the thickness of the specimen.

Two contour maps, obtained with different experimental conditions, are required to determine the values of $\partial u_i / \partial x_i$ and $\partial u_i / \partial x_m$. Contour maps recorded with first and higher order diffraction from P_i may be used (represented by diffraction vectors \underline{h}_i and $n\underline{h}_i$, where n represents the order of diffraction). A second approach is to use different wavelengths and a single diffraction vector. Another method is to use diffraction from \underline{h}_i and $-\underline{h}_i$; the dilational and shear components will produce rotations which will add in one case and will be of the opposite sense in the other.

Referring to the coordinate system in Figure 1, the following terms can be determined as a function of position (x_1, x_3) using the rotation axes and diffraction planes normally used in topography: for diffraction plane P_1 and rotation axis \underline{x}_3 , $\partial u_1 / \partial x_1$ and $\partial u_1 / \partial x_2$ are measured; for diffraction plane P_3 and rotation axis \underline{x}_1 , $\partial u_3 / \partial x_3$ and $\partial u_3 / \partial x_2$ are measured

and for diffraction plane P_2 and rotation axis \underline{x}_1 or \underline{x}_3 , $\partial u_2/\partial x_2$ and $\partial u_2/\partial x_3$ or $\partial u_2/\partial x_1$ are measured.

The strain tensor is not completely defined by these measurements, however, as $\partial u_1/\partial x_3$ and $\partial u_3/\partial x_1$ remain unknown. Measurements with additional rotation axes are required. For diffraction from P_1 (required for determination of $\partial u_1/\partial x_3$), the appropriate rotation axis is \underline{x}_2 . Terms $\partial u_1/\partial x_1$ and $\partial u_1/\partial x_2$ contribute negligibly to the rotation $\Delta\omega_1^2$, and only $\partial u_1/\partial x_3$ has a significant effect. For $\partial u_3/\partial x_1$, diffraction from P_3 and rotation about \underline{x}_2 is required. A check of the internal consistency of the measurements can be provided using the equations of static equilibrium.

III. STRAIN FIELDS AROUND A β -NIOBIUM HYDRIDE PRECIPITATE

The Nb-H system is the paradigm for hydrogen related failure via stress assisted nucleation and fracture of hydride precipitates. Precipitation of β -NbH and accommodation of its 12% volume increase have been investigated with electron microscopy (Makenas and Birnbaum 1980 and Schober 1975) and with optical and scanning electron microscopy (Birnbaum, Grossbeck and Amano 1976). Little information is available, however, on the distribution of elastic and plastic deformation around nearly macroscopic β -NbH precipitates. Conventional x-ray topography is not particularly helpful since the individual dislocations near the precipitate are too closely spaced to be resolved. The contour mapping analysis is suited to this problem, and its

sensitivity to small strains makes it particularly attractive.

III.1. Hydride Precipitate Morphology

Single crystals of niobium with low dislocation densities were obtained by strain annealing polycrystalline ribbons (Stock 1983). Subgrain sizes were quite large: the crystal described below contains a single subgrain with dimensions of 8 mm x 40 mm x 75 μ m. The specimen was charged to a concentration of 3.0 at. % hydrogen, and hydride precipitates were grown during cooling from room temperature in a thermal gradient. Many small hydride precipitates formed at the colder end while larger, well spaced precipitates grew in the warmer portions of the crystal. The hydride precipitates remained intact on warming to room temperature because of the considerable hysteresis in the reversion reaction (Birnbaum et al. 1976). The variation in precipitate size and spacing is shown in Figure 2. Most of the precipitates grew at or near one face of the crystal and did not extend entirely through the crystal.

The larger precipitates were quite irregular with one or two dendritic arms extending in a direction perpendicular to the temperature gradient. The precipitate labeled B in Figure 2 was selected for study because of its isolation. Its two parallel arms consist of inclined stacks of small platelets, each having the expected {100} habit planes (Birnbaum et al. 1976) and dimensions of about 0.1 mm in length and 0.01 mm in width. Elastic energy calculations (Perovic, Purdy and Brown 1981)

suggest that inclined stacks of precipitates will form when the tetragonal component is much greater than the shear component of the transformation strain. This is the case for precipitation of β -NbH from the solid solution (Pick and Bausch 1976).

III.2. Conventional X-ray Diffraction Topography

Lang topography was used to obtain a qualitative understanding of the pattern of deformation and to select a suitable precipitate for analysis before equi-inclination contour mapping was begun. Topographs were recorded with Mo K α radiation and Ilford 50 μ m thick L4 emulsions.

Diffraction vectors $\underline{h} = [002], [1\bar{1}0], [\bar{1}12], [1\bar{1}2]$ and $[0\bar{1}1]$ were used, and $\mu t \approx 1$ where μ is the absorption coefficient and t is the specimen thickness. Topographs were recorded with several incident beam directions for each diffraction vector, and representative topographs are shown in Figure 3. The most prominent features in these topographs are the K α_1 and K α_2 equi-inclination contours. The location of the hydride precipitates is evident from the locally enhanced scattering (i.e., darkening on the topographs) and from the convergence of the K α_1 and K α_2 contours. The outline of the precipitates can be seen in the $\underline{h} = [002], [1\bar{1}0]$ and $[1\bar{1}2]$ topographs (Figure 3a-c).

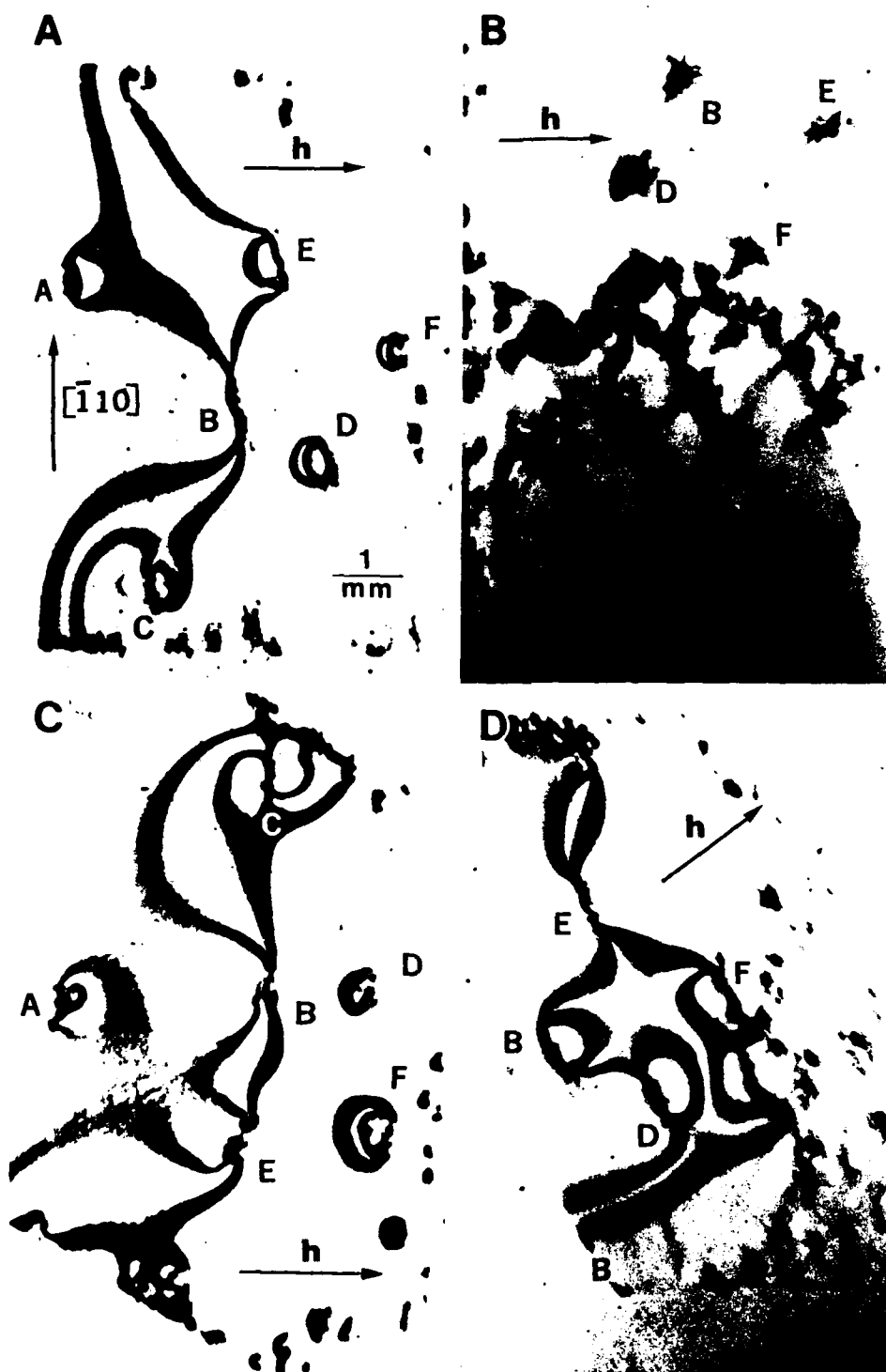
Dislocation images could not be resolved although there were indications of the presence of large numbers of dislocations. Relatively faint half-loops or pairs of half-loops were observed

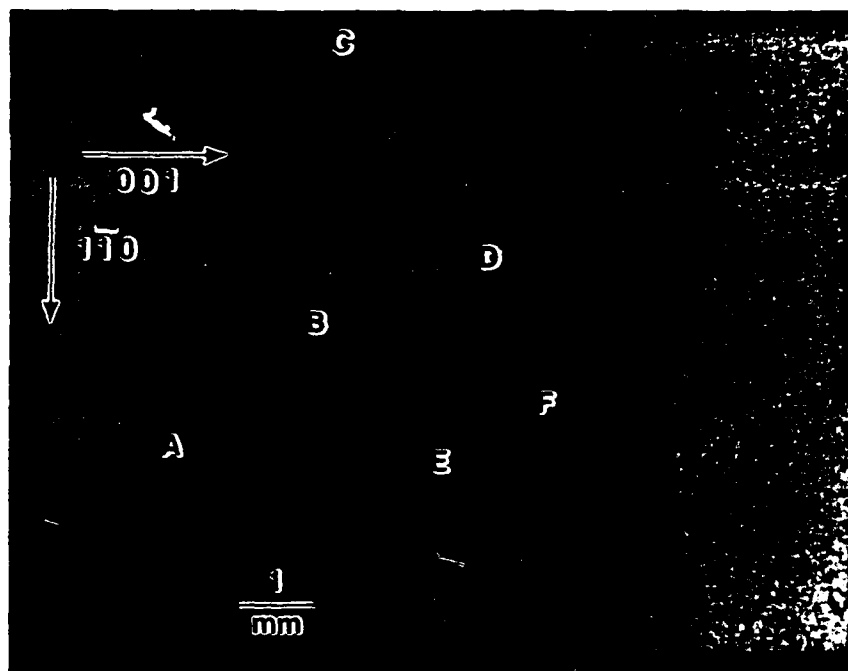
to extend from the hydride precipitates (Figure 3c). The half-loops might be caused by the presence of an array of parallel dislocations with identical Burgers vectors. The diffuse lobes of increased scattering visible in the $h = [1\bar{1}0]$ topograph (Figure 3b) also might indicate the presence of such an excess dislocation density. Similar features have been observed near hardness indentations in copper and MgO single crystals (Armstrong and Wu 1978) and have been interpreted as resulting from a local increase in the excess dislocation density.

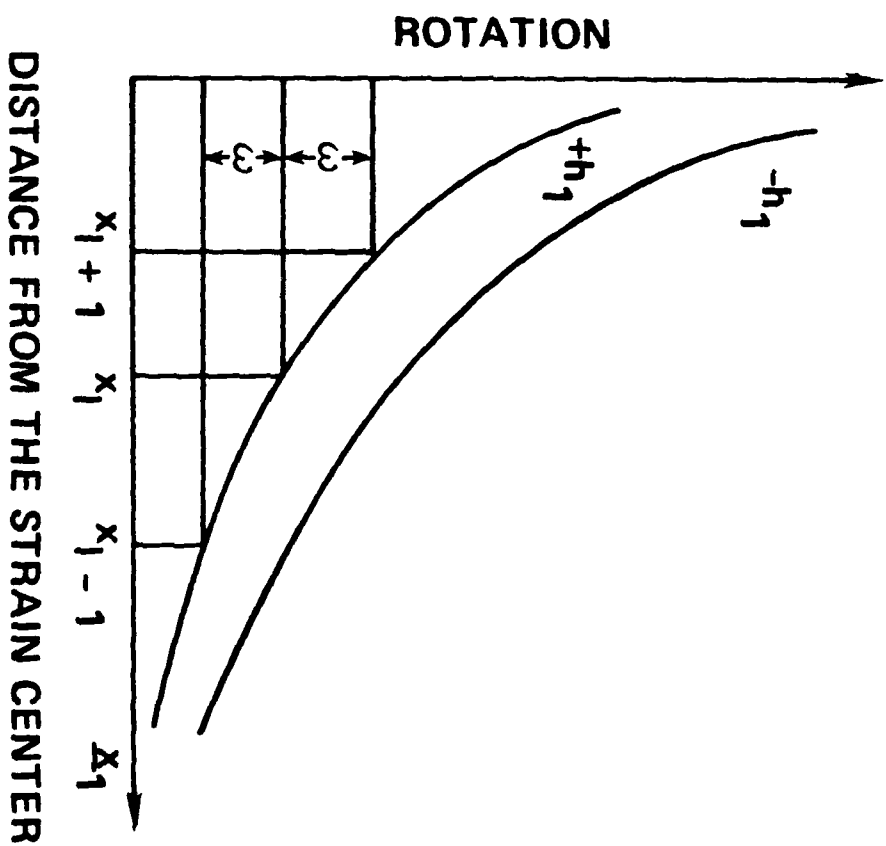
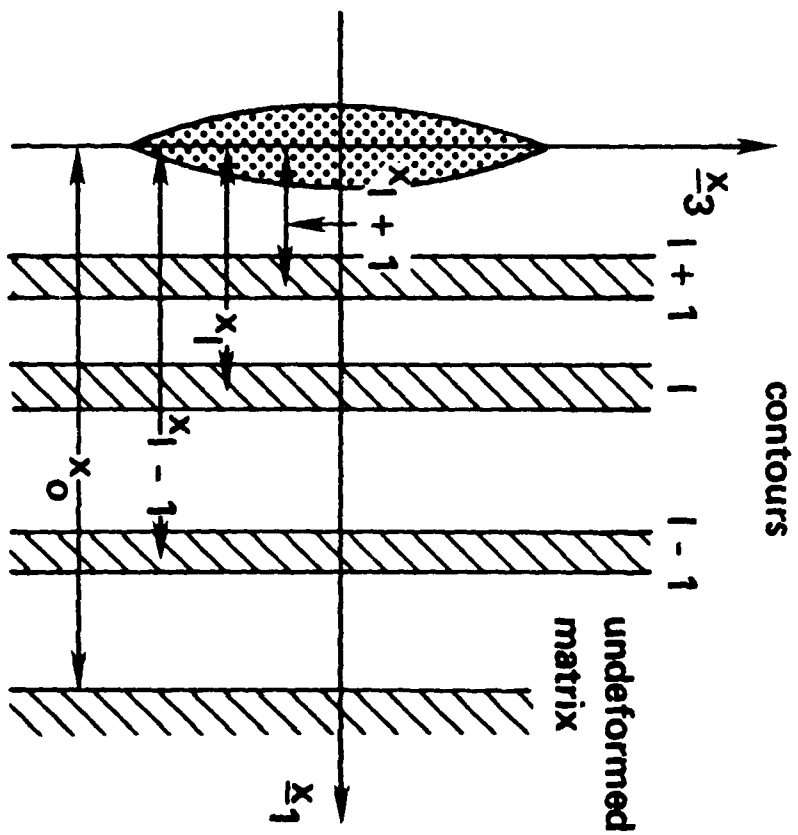
III.3. Equi-Inclination Contour Analysis

Double crystal topography with an asymmetrically cut reference crystal is more suitable for equi-inclination contour mapping than Lang topography. First, the width of the contours is considerably less with the double crystal topography, and greater accuracy in contour position measurements is possible. Second, specimen rotations may be made with greater precision with a double crystal camera. Use of an asymmetric reference crystal allows large cross-sections of the sample crystal to be illuminated simultaneously.

Alignment of the specimen was speeded by the use of a simple x-ray image intensifying system. Maximum spatial resolution, however, required exposure of film. The single exposure topographs were recorded on Kodak PF57 dental film while multiple exposure topographs were recorded on 50 μm Ilford L4 nuclear emulsions: the dental film has adequate resolution for contour







- Figure 5. Single exposure double crystal topographs recorded with diffraction vector $[\bar{1}10]$. Specimen rotations of 140 arc sec. about the axis $[001]$ were used to produce these topographs.
- Figure 6. Position of the center of the contours. (a) $\underline{h} = [\bar{1}10]$ and (b) $\underline{h} = [1\bar{1}0]$. The inset drawing shows the relationship between the precipitate orientation and the contour map.
- Figure 7. Rotation as a function of distance from the hydride center along the \underline{x}_3 axis. The curves obtained using $\pm \underline{h}$ are offset for clarity.
- Figure 8. The two-dimensional variation of (a) $\partial u_3 / \partial x_3$ and (b) $\partial u_3 / \partial x_2$ around the hydride precipitate.
- Figure 9. Absorption edge contours in a lightly deformed niobium crystal. The topographs were recorded with diffraction vector $[002]$ and rotations of 90 arc sec. between exposures.
- Figure 10. A multiple exposure, double crystal topograph of a notched niobium crystal after tensile loading. The interaction between the plastic zone and a neighboring subgrain is shown by the large number of equi-inclination contours linking the two features. The subgrain is indicated by S and the notch by N.

FIGURE CAPTIONS

- Figure 1. The relationship between contour positions and specimen rotation. (a) Contours on a topograph recorded with diffraction from planes P_1 and rotations about x_3 by increments of ω . (b) The relationship between contour position and cumulative rotation for contours obtained with $\pm h_1$. The former is measured relative to the strain center and the latter relative to the specimen orientation at which the undeformed regions of the crystal diffract.
- Figure 2. A low magnification optical micrograph of the specimen showing the distribution of hydride precipitates.
- Figure 3. Lang topographs showing deformation of the niobium matrix following the formation of the β -NbH precipitates. Topographs were obtained with diffraction vectors: (a) $[002]$, (b) $[1\bar{1}0]$, (c) $[1\bar{1}2]$ and (d) $[11\bar{2}]$.
- Figure 4. Multiple exposure double crystal topograph showing the arrangement of contours surrounding precipitate B. The diffraction vector was $[002]$, and the contours were produced by specimen rotations of 210 arc sec. about the $[\bar{1}10]$ axis.

REFERENCES

- Armstrong, R. W. and Wu, C. Cm., Lattice misorientation and displaced volume for microhardness indentations in MgO crystals, J. Am. Cer. Soc. 61: 102 (1978).
- Birnbaum, H. K., Grossbeck, M. L. and Amano, M., Hydride precipitation in Nb and some properties of NbH, J. Less-Common Metals, 49: 357 (1976).
- Bonse, U. and Hartmann, I., X-ray measurement of minute lattice strain in perfect silicon crystals, Z. Kristall. 156: 265 (1981).
- Bowen, D. K., Stock, S. R., Davies, S. T., Pantos, E., Birnbaum, H. K. and Chen, Haydn, Topographic EXAFS, Nature 309: 336 (1984).
- Hart, M., Bragg angle measurement and mapping, J. Cryst. Growth 55: 409 (1981).
- Jacobs, L. and Hart, M., An x-ray topographic study of large crystals for a bent-crystal gamma diffractometer, Nuc. Instr. Methods 143: 319 (1977).
- Liu, H. Y., Weng, G. Y. and Weissmann, S., Determination of notch-tip plasticity by x-ray diffraction and comparison to continuum mechanics analysis, J. Appl. Cryst. 15: 594 (1982).
- Makenas, B. J. and Birnbaum, H. K., Phase changes in the niobium-hydrogen system I: Accommodation effects during hydride precipitation, Acta Metall. 28: 979 (1980).
- Perovic, V., Purdy, G. R. and Brown, L. M., The role of shear transformation strains in the formation of linear arrays of precipitates, Scr. Met. 15: 217 (1981).
- Pick, M. A. and Bausch, R., The determination of the force-dipole tensor of hydrogen in niobium, J. Phys. F: Metal Phys. 6: 1751 (1976).
- Renninger, M., Beitrage zur doppeldiffraktometrischen Kristall-Topographie mit Rontgenstrahlen I. Methodik und Ergebnisse typischer Art, Z. angew. Physik 19: 20 (1965).
- Schober, T., The niobium-hydrogen system--an electron microscope study II. low-temperature structures, Phys. Stat. Sol (a) 30: 107 (1975).
- Stock, S. R., X-ray topographic studies of deformation in niobium and dilute niobium-hydrogen alloys, Ph.D. thesis, University of Illinois at Urbana Champaign (1983).

precipitate of β -NbH in a single crystal of niobium. The complex precipitate morphology and the lack of distinct topographic images of it complicated the analysis. These two factors contributed most of the uncertainty and estimated error in the present measurements. Use of synchrotron white radiation and absorption edge contours allow an image of the precipitate to be obtained on each topograph and promise improvements in the precision with which measurements can be made.

We anticipate a number of applications of the contour mapping technique. Besides precipitate strain field analysis, this technique might be applied to the strain fields surrounding hardness indentations or to plastic zones spreading from notches during tensile loading.

ACKNOWLEDGEMENTS

This work was part of the Ph.D. thesis of S. R. Stock (University of Illinois, 1983) and was supported by the Office of Naval Research through contract N00014-75-C-1012. One of the authors (SRS) would also like to acknowledge support from a graduate fellowship provided by IBM. We would also like to acknowledge use of the facilities of the MRL Center for Microanalysis of Materials which is supported as a national facility by the Materials Sciences Division of the Department of Energy.

specimens if a filter is placed between the specimen and the recording medium. The specimen diffracts a range of wavelengths across its width and an appropriate filter material and thickness may be chosen to provide the needed absorption contrast. One can imagine dynamic experiments where contour patterns are required from several different diffraction spots during a short period of time. A different filter could be used with each diffraction spot, and the experiment could be performed with dispatch.

IV. SUMMARY

An x-ray topography technique has been outlined for quantifying the distribution and magnitude of deformation in single crystal specimens. Equi-inclination contour and absorption edge contour mapping, the basis of this method, combine spatial discrimination with the sensitivity to small strains of x-ray diffraction. The contour analysis is applicable to both plastic and elastic deformation fields and is particularly powerful in applications where plastic deformation is too great for conventional x-ray topographic imaging and where the spatial extent of the deformation fields is too large to study with transmission electron microscopy.

An example of equi-inclination contour analysis is presented, illustrating the complications and practical limitations of this technique. Two of the nine terms $\partial u_i / \partial x_j$ of the strain tensor were measured as a function of position about a

crystal which was deformed plastically under tensile loading. The double crystal topograph was recorded with a laboratory source of Mo K α radiation, and a number of equi-inclination contours were required to form the image. Considerable interaction between the plastic zone and a neighboring subgrain can be seen. The image of the plastic zone is serrated, and it is unclear whether this is an artifact of the multiple exposure contour mapping. To what extent the large strains within the plastic zone will broaden the equi-inclination contours and limit resolution remains to be determined. It appears, however, that absorption edge contour mapping would be superior in studies of deformation at notches since the drastic change in absorption coefficient leads to a very sharp contour.

Not all single crystals can be directly studied with absorption edge contours since the range of wavelengths of synchrotron x-radiation with appreciable intensity is limited by two factors. At higher wavelengths there is attenuation of the beam due to the beryllium windows; at lower wavelengths there is a rapid decrease in intensity which is an intrinsic feature of synchrotron radiation. Absorption edge contours can only be obtained from the specimen if there was sufficient concentration of an element with an absorption edge in the appropriate range of energies (which would depend on the specific storage ring or synchrotron used). Apparently, materials such as silicon ($\lambda_{\text{edge}} = 6.74\text{\AA}$) cannot be studied with this technique. Contour mapping with absorption edges is possible, however, for such

reliable than the variation, as a function of position, of a single term. At any position (x_1, x_3) the strain components must satisfy the equations of static equilibrium, and the internal consistency of measurements can readily be assessed.

It should be noted that $\partial u_i / \partial x_{j \neq i}$ measured by equi-inclination contour mapping does not reflect the total dislocation density. What is measured is $(\partial u_i / \partial x_{j \neq i})_{xs}$, the component due to the excess dislocation density of a given character. The total dislocation density and, hence, the total strain can be much larger. The terms $\partial u_i / \partial x_i$ do, however, reflect the total dislocation density. In cases such as the precipitation of β -NbH where the plastic deformation is primarily from the punching of prismatic dislocation loops, the difference between $(\partial u_i / \partial x_j)_{xs}$ and $(\partial u_i / \partial x_j)_{total}$ should be unimportant.

III.4. Absorption Edge Contours

The use of white radiation and absorption edge contours should ease comparison between different reflections since images are obtained from the entire crystal. Figure 9 shows absorption edge contours of a lightly deformed niobium crystal which were produced with diffraction vector $\underline{h} = [002]$ and with rotations of 90 arc seconds (Bowen, Stock, Davies, Pantos, Birnbaum and Chen 1984).

Another advantage of absorption edge contours is their sharpness. Figure 10 shows a topograph of a notched niobium

curves of Figure 7 (after removing the artificial offset). The point at which the slopes of the two curves differ is the point where the magnitude of the dilational strain is greater than zero. Once the rotation due to dilation $\partial u_3 / \partial x_3$ is known, and a correction for macroscopic bending is made, the rotation due to shear may be determined. Figure 8 shows the two-dimensional variation of $\partial u_3 / \partial x_3$ and $\partial u_3 / \partial x_2$ around the hydride precipitate. Near the precipitate the magnitude of $\partial u_3 / \partial x_3$ is greater than $\partial u_3 / \partial x_2$; however, the dilational field decreases more rapidly than the shear field, particularly along the direction $x_1 = [001]$, so that the shear contribution dominates farther away from the precipitate. The value of $\partial u_3 / \partial x_3$ at ($x_1 = 0$, $x_3 = 350 \mu\text{m}$) is $4.2 (+0.7, -1.1) \times 10^{-3}$ while the value of $\partial u_3 / \partial x_2$ is $2.4 (+0.3, -0.2) \times 10^{-3}$. The uncertainty in $\partial u_3 / \partial x_3$ is larger because of the factor of $\tan \theta_0$ which relates $\Delta \theta_D$ to the dilational strain.

The inter-contour spacings from any single reflection are more reliable than comparisons between reflections since the reference position will vary little for the rotations used. This can be seen in Figure 7 where there is little deviation of the individual points from the average curves. It is difficult, however, to identify the center of deformation for the comparison of different reflections. The indistinct double image of precipitate B in the $\underline{h} = [002]$ topographs corresponds to the precipitate's arms, and no other features can be resolved. Therefore, the absolute magnitudes $\partial u_i / \partial x_j$ are somewhat less

portion of the precipitate.

Contour maps recorded with $\underline{h} = [\bar{1}10]$ and $[1\bar{1}0]$ and with rotation axis $[001]$ were used to determine $\partial u_3/\partial x_2$ and $\partial u_3/\partial x_3$. Figure 7 shows rotation as a function of distance from the hydride center along $x_1 = 0$ for $x_3 < 0$. The curves for \underline{h} and $-\underline{h}$ are offset for clarity, and the estimated errors (± 3 arc sec. rotation and $\pm 20 \mu\text{m}$ for contour positions) are smaller than the size of the data points. The dashed vertical line represents the center of the hydride image.

In determining the strain field due to a discrete feature one must make allowance for any strains which may have been present in the sample prior to the feature's formation. Initially, the crystal studied here was uniformly bent about axis $[001]$ with a radius of curvature of about 0.5 m. If rotation were plotted as a function of contour position, the slope of the curve would be constant. The growth of each precipitate superimposed an additional deformation field over the macroscopic bending. Therefore, the position of vanishing strain from the precipitate is that where the slope of the rotation vs. distance curve matches that of the macroscopic bending. The dash-dotted line in Figure 7 represents the curvature due to the macroscopic bending, and, as expected, the graphs of rotation versus contour position follow this slope at distances x_3 greater than about 1.0 mm from the center of the hydride precipitate.

The dilational contribution is determined from the difference in rotation (in radians) between the $\underline{h} = \pm[\bar{1}10]$

left for the contours on the left and vice versa. Little shift in the precipitate images were observed from topograph to topograph for the contours shown in Figure 5. Considerable translation of the precipitate image was seen, however, in the topographs recorded during the rotation of 1120 arc sec. between the outermost contours plotted in Figure 6. The total shift of this image was about 300 μm and was associated solely with those contours which did not close upon themselves.

Contours were also recorded inside those of Figure 6. Their positions changed little with each increment of rotation; and the broad precipitate and contour images merged. These contours cannot be used in the analysis since the uncertainty in the contour position is comparable to contour-contour separation. The area enclosed within the innermost contour was slightly less than the length and width measured by optical microscopy, 800 and 250 μm , respectively.

As indicated in Figure 6, the parallel arms of precipitate B are parallel to x_3 and are on the $x_3 < 0$ side while the blocky portion of the precipitate is on the $x_3 > 0$ side. The irregular morphology is reflected in the asymmetry of the contours in Figures 5 and 6. For example, the contours in the lower left quadrant ($x_1, x_3 < 0$) are farther from the precipitate center line because the lower arm of the precipitate extends farther than the upper one. The innermost contours are more closely spaced on the right side than on the left side of the precipitate because of the greater deformation near the larger, blocky

mapping while requiring considerably shorter exposure times.

Equi-inclination contours surrounding precipitate B were recorded using reflection and transmission topography for rotations about $[\bar{1}10]$ and $[001]$ axes. Multiple exposure and rotations of 210 arc sec. were used to produce the transmission topograph shown in Figure 4. Deflection of contours between neighboring precipitates shows that the strain field extends two or three millimeters. The magnitude of deformation near precipitate B is evident: the range of diffraction is greater than 0.3° , and the $K\alpha_1$ and $K\alpha_2$ contours cannot be resolved. The rotation produced by the precipitate is opposite to that of the general curvature of the crystal.

A set of single exposure transmission topographs appears in Figure 5 for diffraction vector $\underline{h} = [\bar{1}10]$, rotation axis $[001]$ and rotation increments of 140 arc sec. Only contours on one side of precipitate B are shown although contours were also recorded on the other side of it. There is an inherent difficulty in constructing contour maps from single exposure topographs of heavily deformed specimens. Contour positions should not be measured relative to the precipitate image since different portions of the precipitate form the image at different specimen orientations. Instead, one should use the image of the edge of the crystal as the reference position.

Figure 6 shows the contour positions on both sides of precipitate B for the topographs recorded with $\underline{h} = [\bar{1}10]$. The two dashed lines represent the precipitate images, that on the

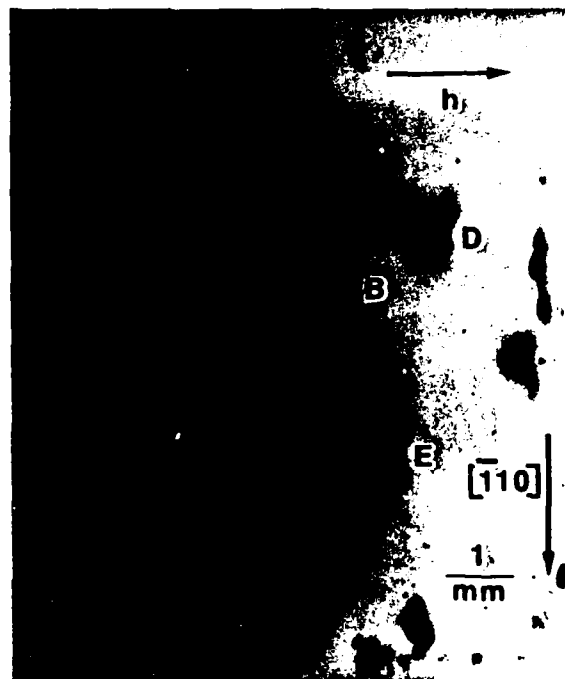


FIG. 4

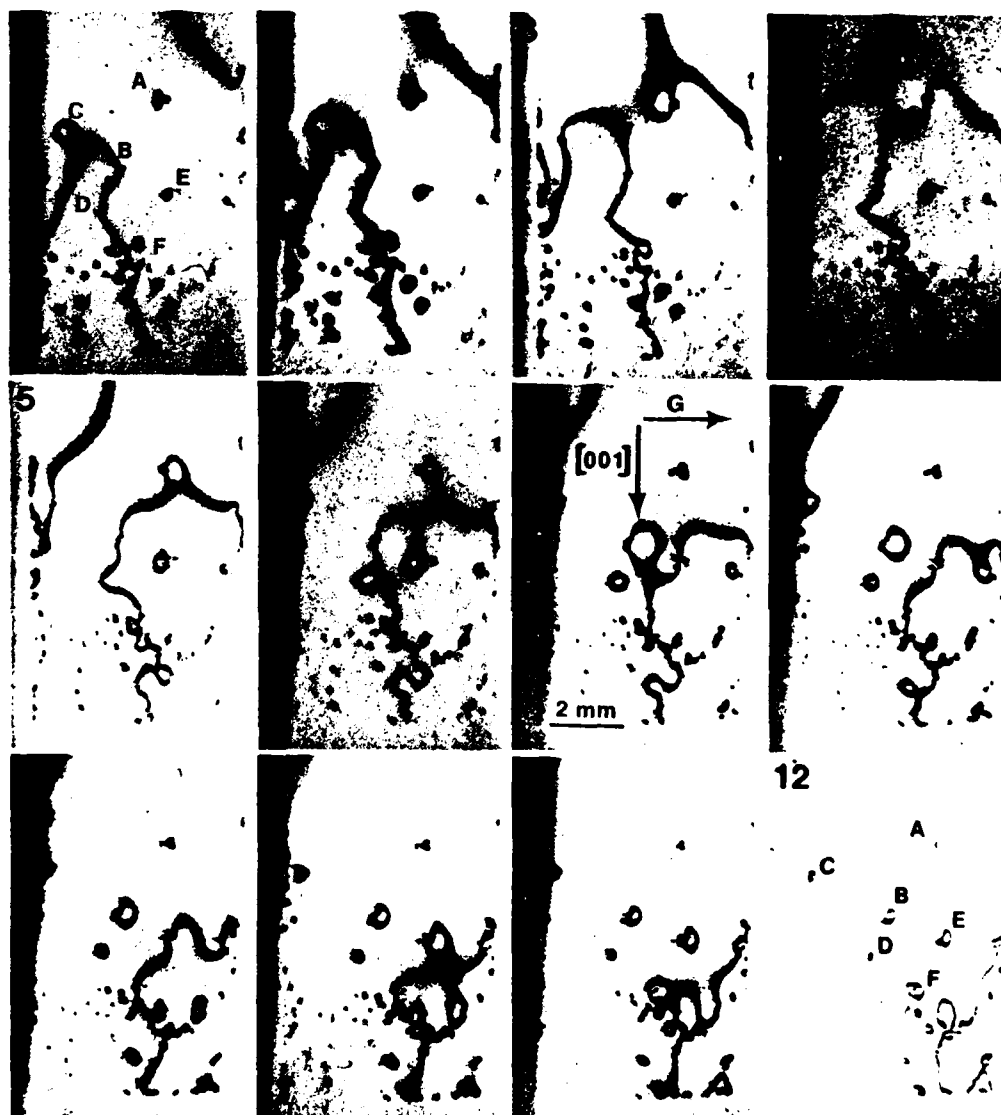
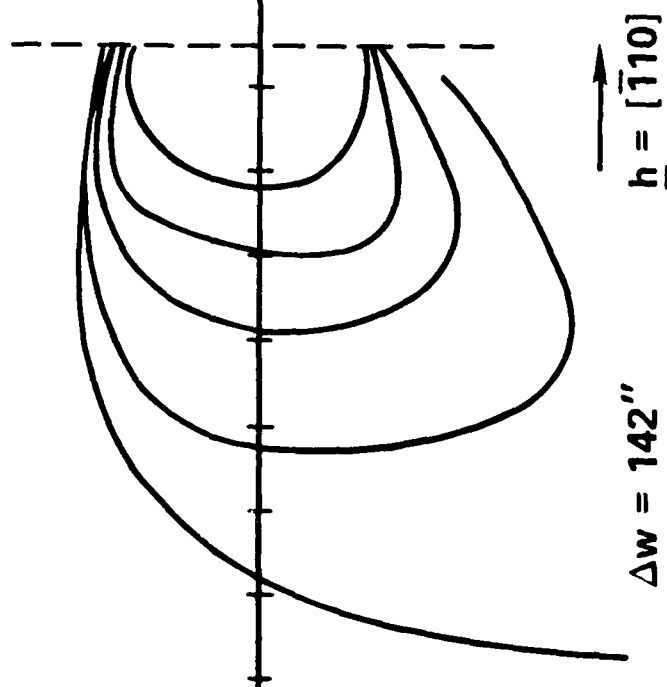
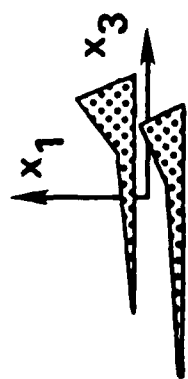
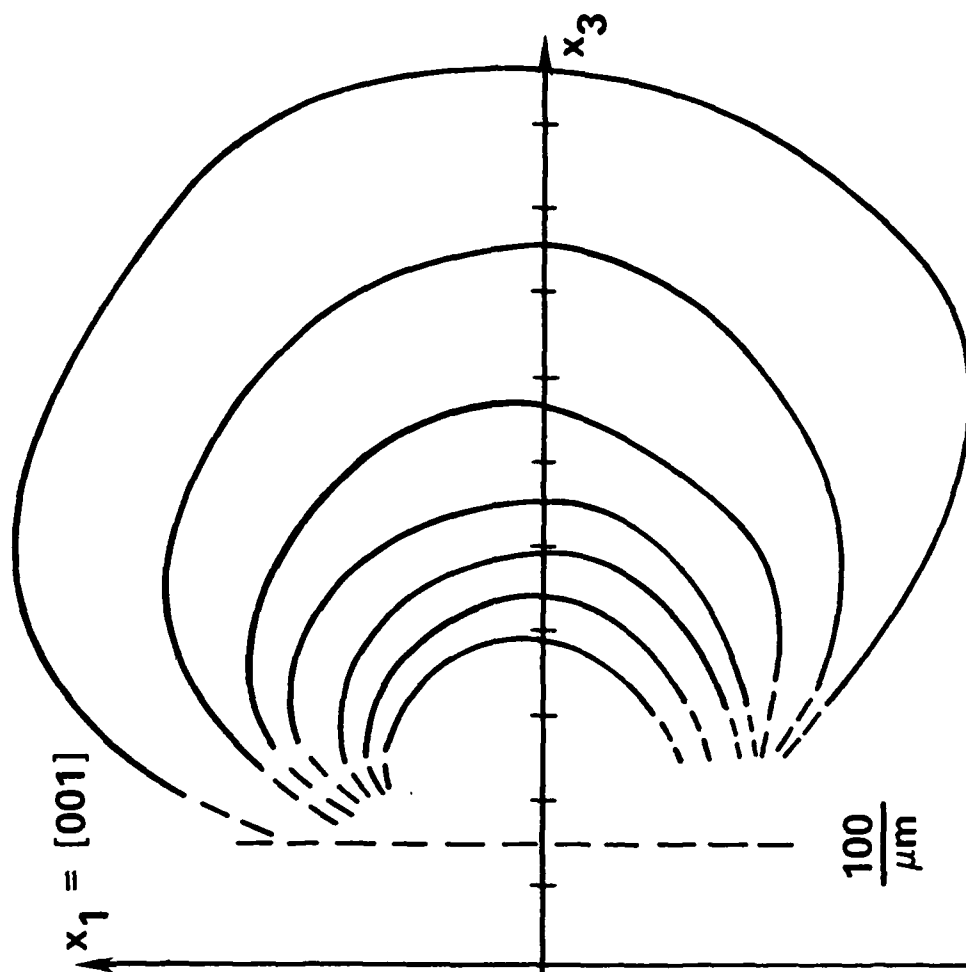
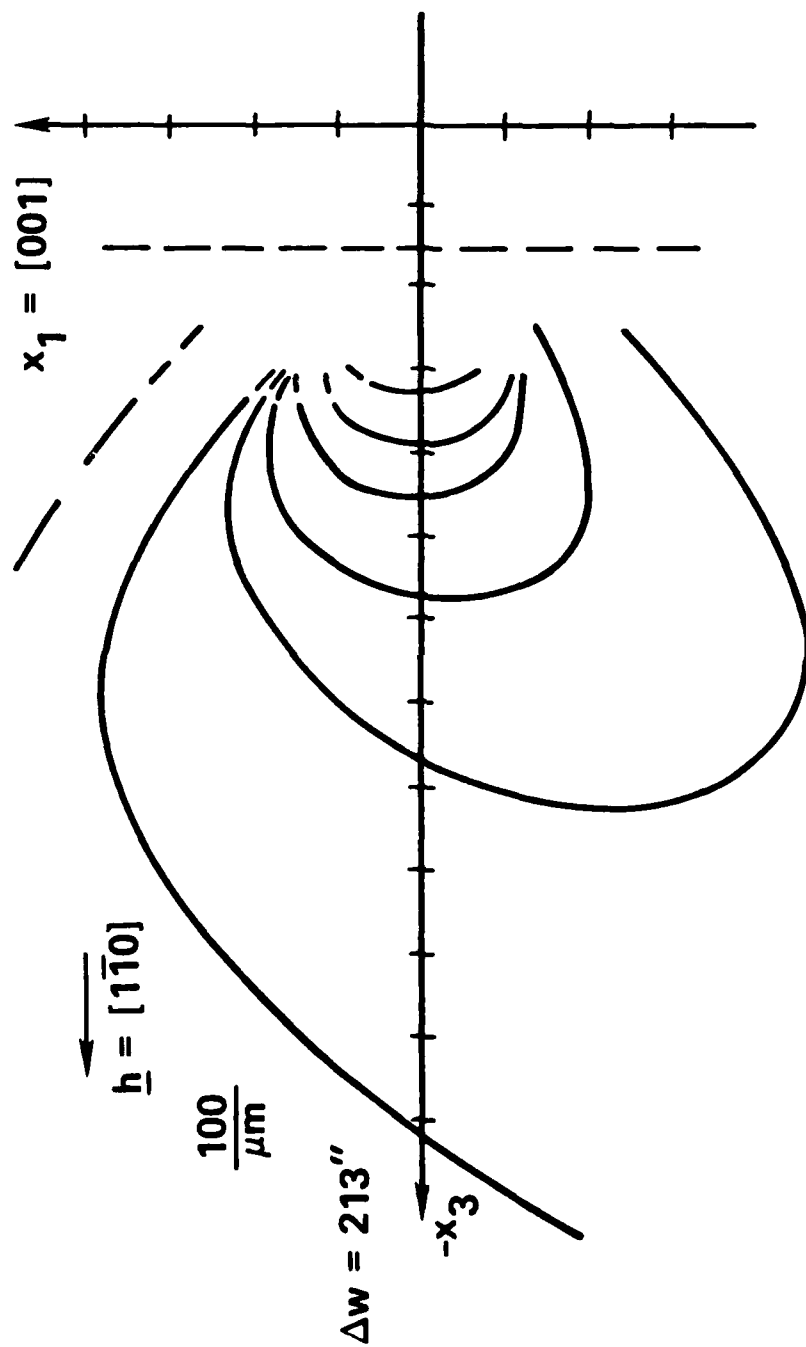
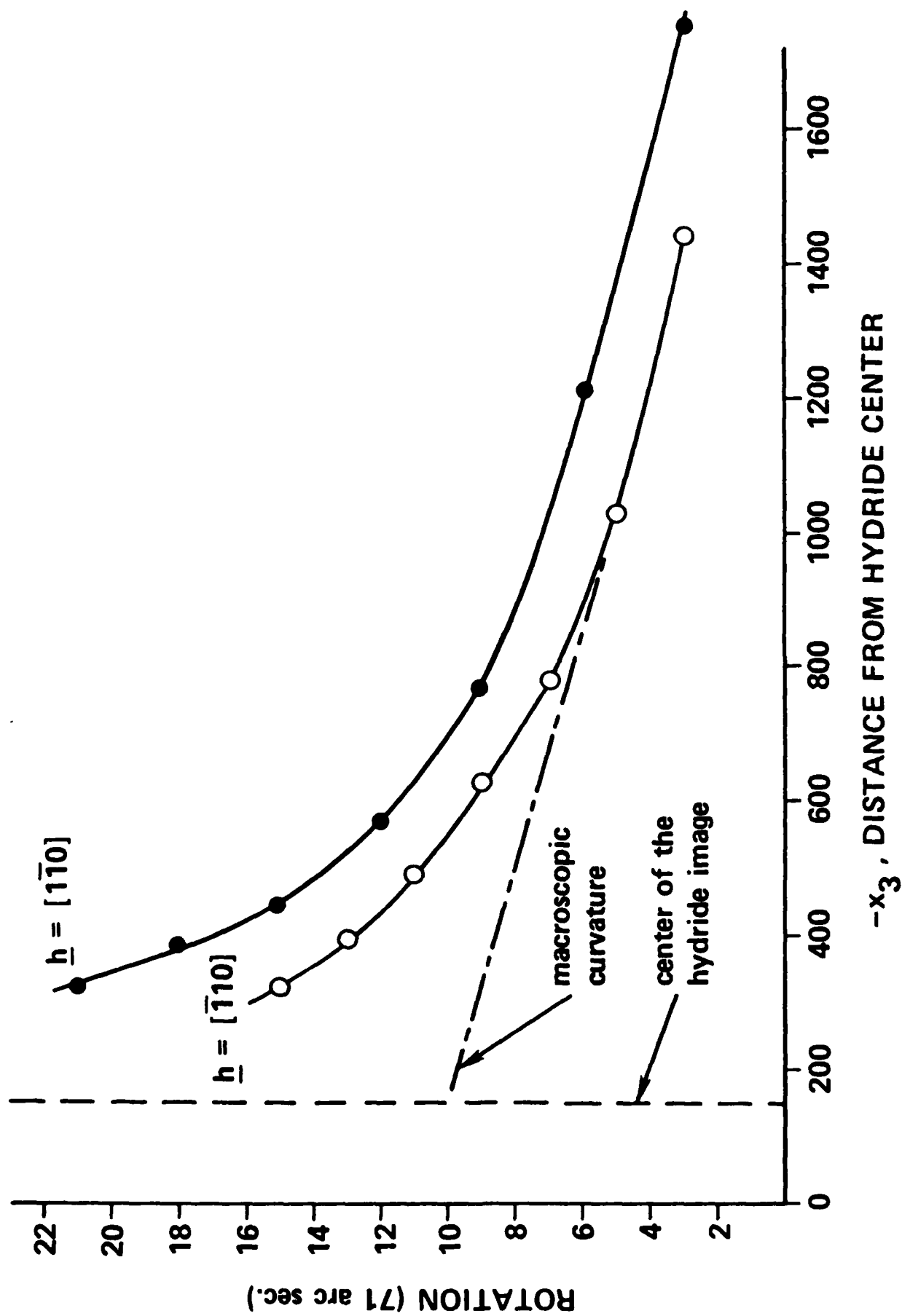
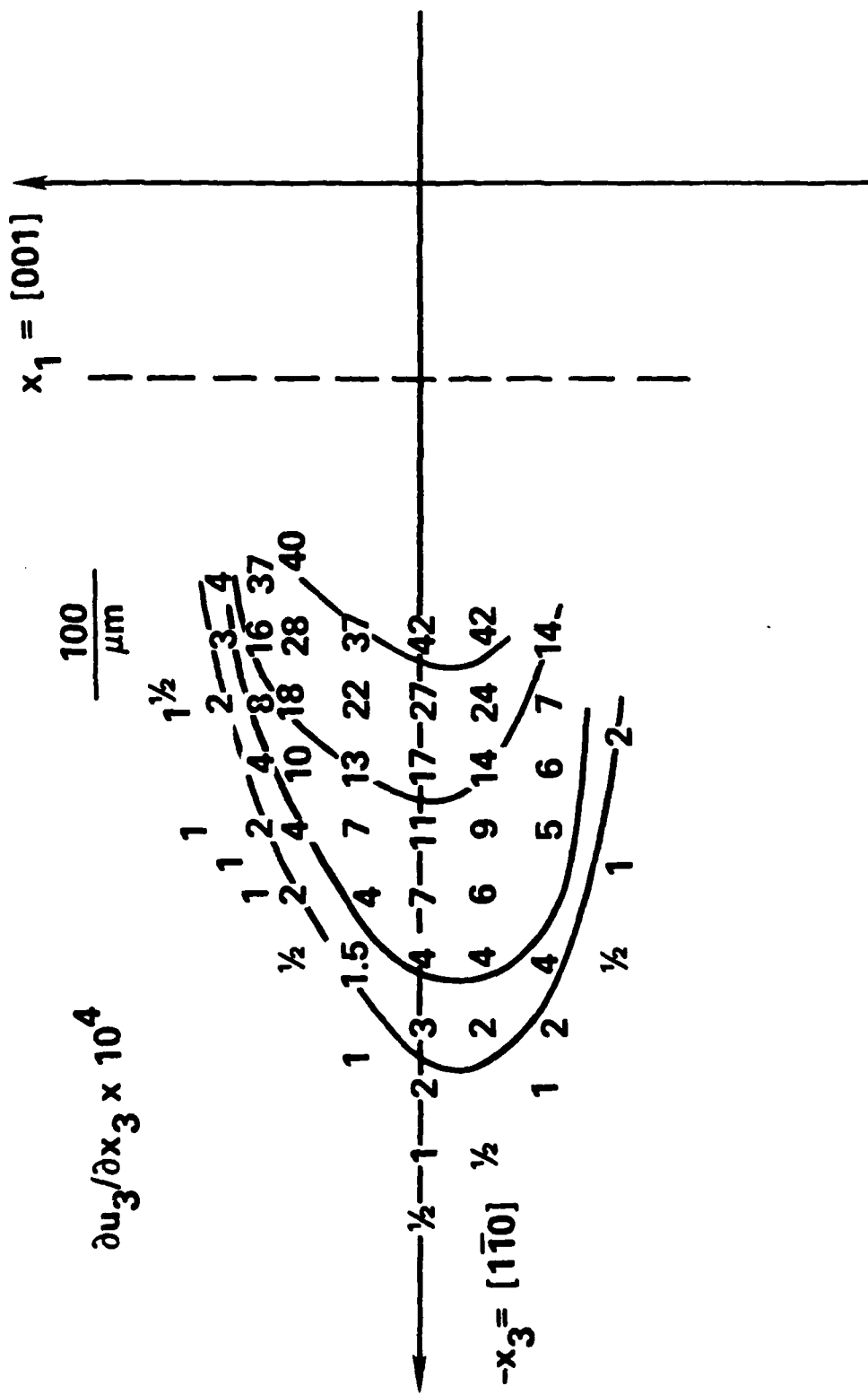


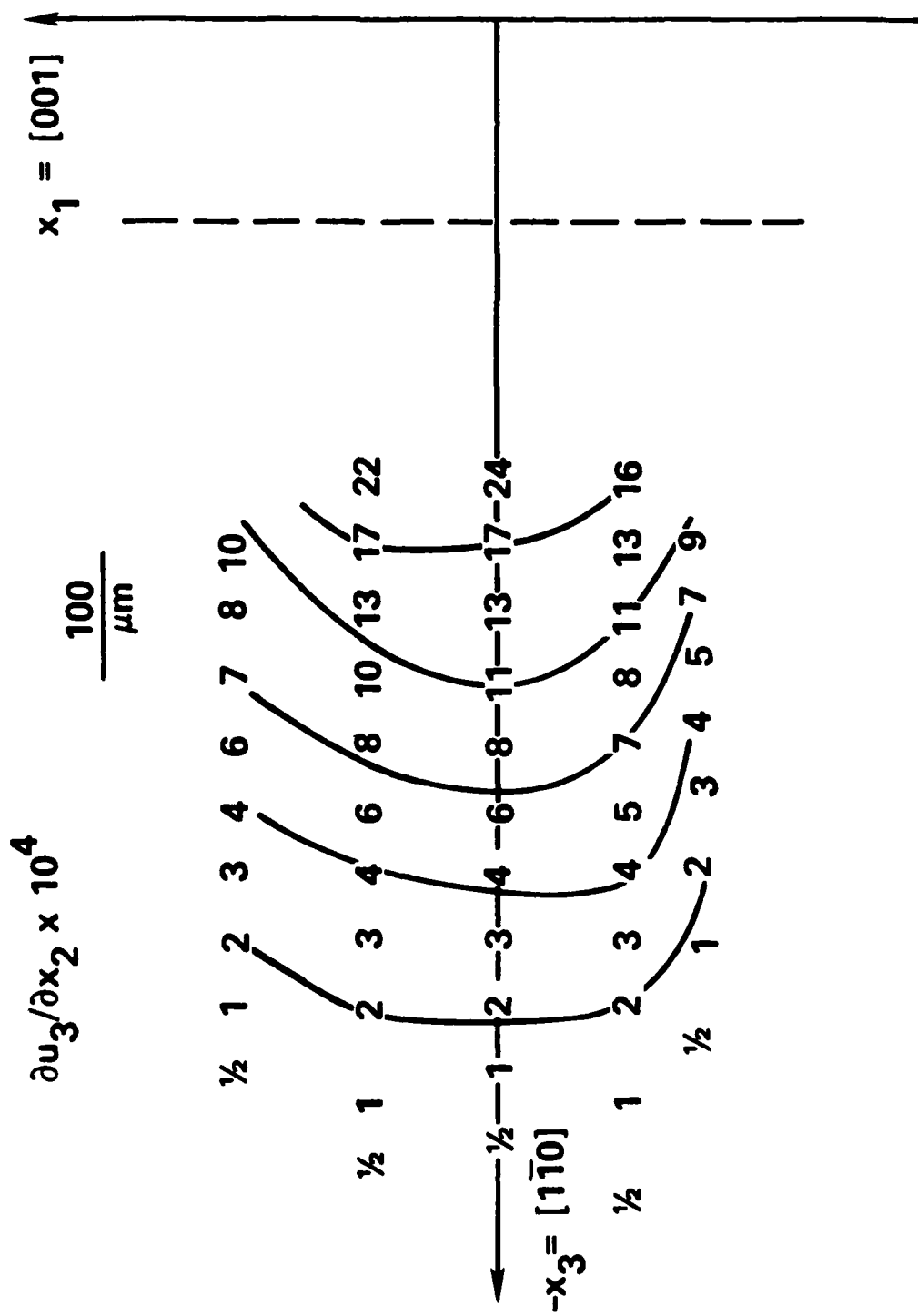
FIG. 5













10



11



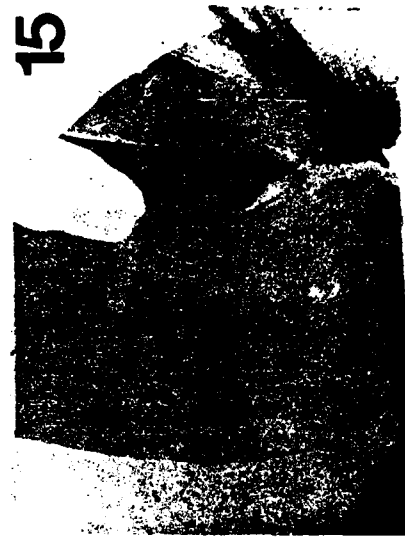
12



13



14



15



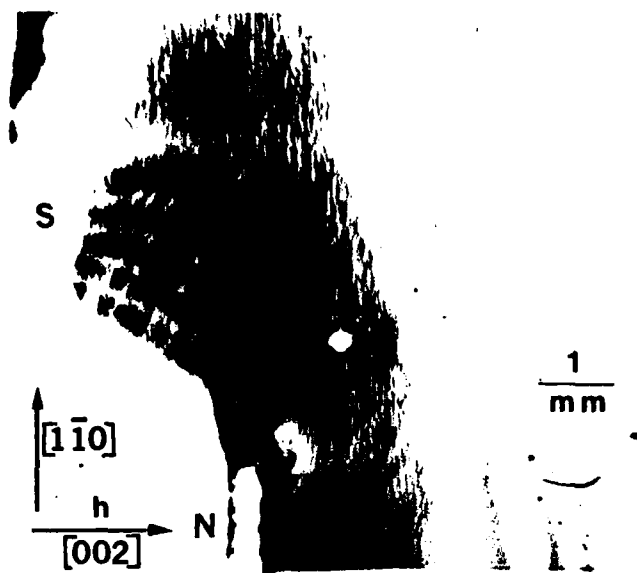
16



17



17E



Unclassified
Security Classification

DOCUMENT CONTROL DATA - R&D

(Security classification of title, body of abstract and indexing annotation must be entered when the overall report is classified)

1. ORIGINATING ACTIVITY (Corporate author) University of Illinois		2a. REPORT SECURITY CLASSIFICATION Unclassified	
		2b. GROUP	
3. REPORT TITLE The Measurement of Strain Fields by X-Ray Topographic Contour Mapping			
4. DESCRIPTIVE NOTES (Type of report and inclusive dates) Technical Report			
5. AUTHOR(S) (Last name, first name, initial) Stock, S.R., Chen, Haydn, Birnbaum, H.K.			
6. REPORT DATE May 1985	7a. TOTAL NO. OF PAGES 31	7b. NO. OF REFS 13	
8a. CONTRACT OR GRANT NO. USN00014-83-K-0468		9a. ORIGINATOR'S REPORT NUMBER(S)	
b. PROJECT NO.			
c.		9b. OTHER REPORT NO(S) (Any other numbers that may be assigned this report)	
d.			
10. AVAILABILITY/LIMITATION NOTICES This document is unclassified. Reproduction and distribution for any purpose of the U.S. Government is permitted. Approved for public release Distribution Unlimited			
11. SUPPLEMENTARY NOTES		12. SPONSORING MILITARY ACTIVITY Office of Naval Research	
13. ABSTRACT <p>An x-ray topographic method is described for measuring the magnitude of the components of the strain tensor as a function of position in single crystal specimens. Several variants of the technique are described for use with monochromatic or white x-radiation. Results are reported for some components of the deformation field surrounding a precipitate of β-NbH. Possible applications of contour mapping are discussed.</p>			

DD FORM 1473
1 JAN 64

Unclassified

Security Classification

END

FILMED

7-85

DTIC